Supporting Information

A Self-Templating Redox-Mediated Synthesis of Hollow Phosphated Manganese Oxide Nanospheres as Noble-Metal-like Oxygen Electrocatalysts

Tianran Zhang, †, ‡ Shengliang Zhang, †, ‡ Sheng Cao, †, ‡ Qiaofeng Yao † and Jim Yang Lee *, †, ‡

† Department of Chemical and Biomolecular Engineering, National University of Singapore, 4 Engineering Drive 4, Singapore, 117576, Singapore. E-mail: cheleejy@nus.edu.sg

‡ Cambridge Centre for Advanced Research and Education in Singapore, 1 Create Way, Singapore 138602, Singapore

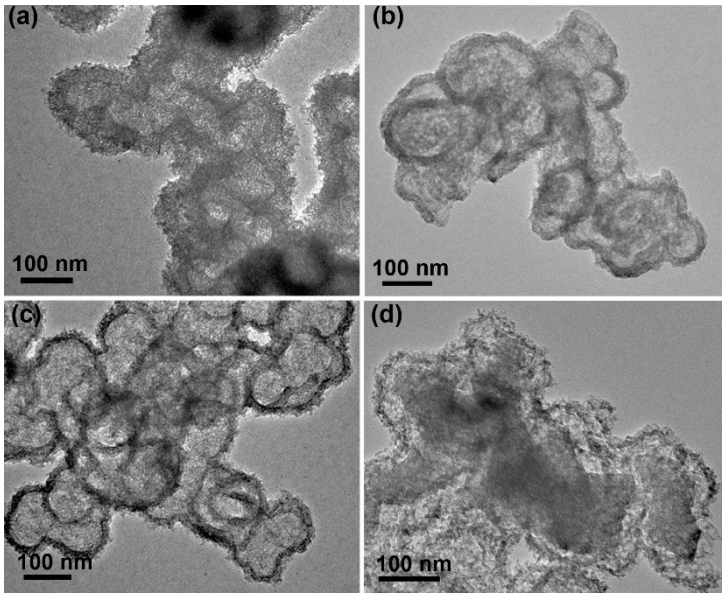

Figure S1. TEM images of h-MnO_xP_y prepared using different $NH_4H_2PO_4$ amounts. (a) 50 mg, (b) 100 mg, (c) 125 mg and (d) 200 mg. The hollow nanostructure was obtained when the amount of $NH_4H_2PO_4$ was below 125 mg. For 200 mg of $NH_4H_2PO_4$, a yolk-shell structure was formed. The shell was h-MnO_xP_y and the core was unreacted manganese phosphate-hydrogen phosphate precursor.

Table S1. Elemental compositions of h-MnO_xP_y.

	Mn	P	O	K
h-$MnO_xP_{0.08}$	22.6	1.79	73.8	1.81
h-$MnO_xP_{0.16}$	22.2	3.56	72.4	1.84
h-$MnO_xP_{0.21}$	26.4	5.53	67.1	0.970
h-$MnO_xP_{0.59}$	15.1	8.86	75.5	0.540

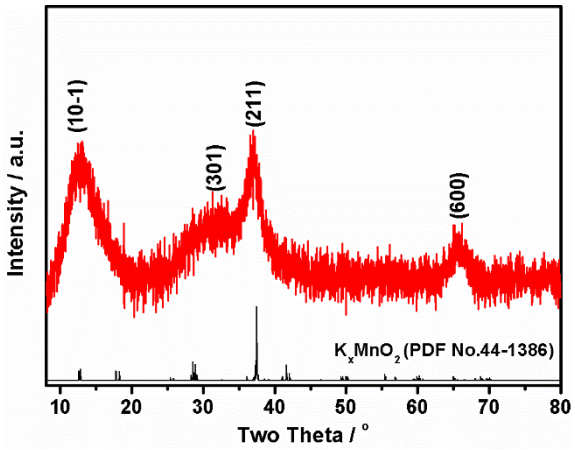

Figure S2. XRD pattern of h-$MnO_xP_{0.21}$.

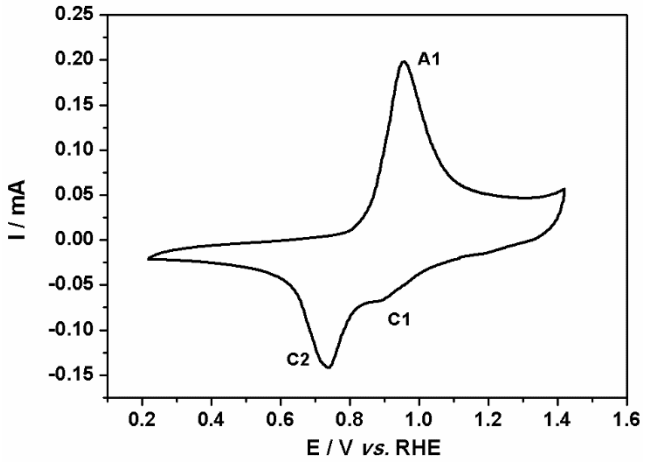

Figure S3. Cyclic voltammetry of h-$MnO_xP_{0.21}$ in Ar-saturated 0.1 M KOH solution with scan rate of 2 mV s^{-1}.

As shown in Figure S3, there are two cathodic peaks located at 0.87 V vs. RHE (C1) and at 0.73 V vs. RHE (C2), which could be attributed to the conversion of Mn (IV) to Mn (III) and of Mn (III) to Mn (II)

(or Mn_3O_4) respectively.[1] In the anodic scan, the large peak at 0.95 V vs. RHE (A1) could be attributed to the formation of Mn (III) from Mn (II) oxidation. No peak for the conversion of Mn (III) to Mn (IV) was detected, probably due to a rising background current (from OER). The dominant Mn (III)/Mn(II) redox features in the voltammogram corroborated the existence of Mn(III) in h-$MnO_xP_{0.21}$.

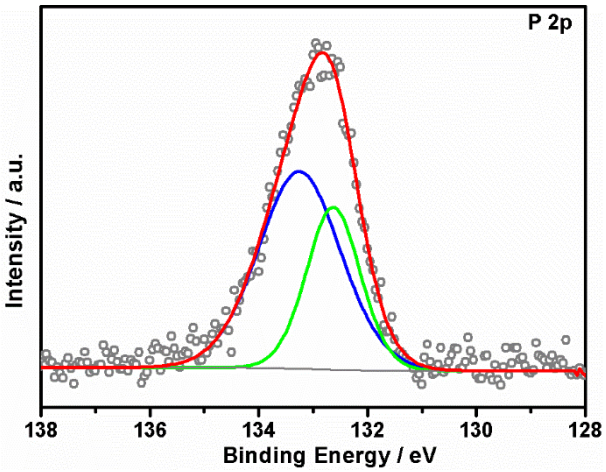

Figure S4. P 2p XPS spectrum of h-$MnO_xP_{0.21}$.

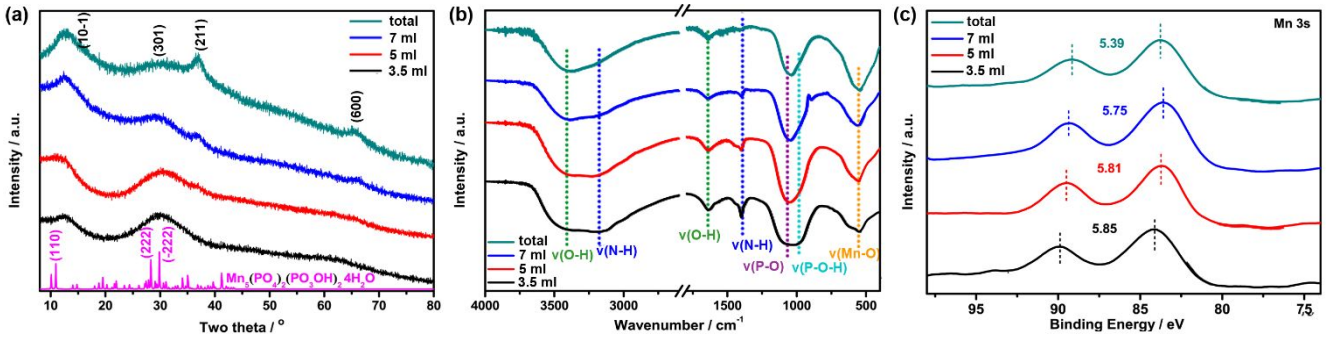

Figure S5. (a) XRD, (b) FT-IR spectra and (c) Mn 3s XPS spectra of the reaction products after the addition of 3.5 ml (black), 5 ml (red), 7 ml (blue), and all (green) of $KMnO_4$ solution to the $MnSO_4$/ $NH_4H_2PO_4$ mixture.

The two broad peaks at ~12 ° and 30° in Figure S4a for the initial porous nanoparticles agree well with the XRD patterns of $Mn_5(PO_4)_2(PO_3OH)_2$ $4H_2O$. FT-IR spectroscopy confirmed the presence of N-H, O-H, P-O and P-O-H moieties in these porous nanoparticles (Figure S4b, black line). Therefore, the porous nanoparticles are referred to as ammonium manganese phosphate-hydrogen phosphate. As the reaction progressed on, two peaks at 38° and 65°, corresponding to the formation of phosphated manganese oxide, were detected by XRD. FT-IR spectroscopy also detected the formation of phosphated manganese oxide

as an increase in the intensity of the Mn-O vibration (Figure S4b). The Mn chemical state was 3+ in the final product, indicating the oxidization of the Mn (II) by $KMnO_4$ (Figure S4c).

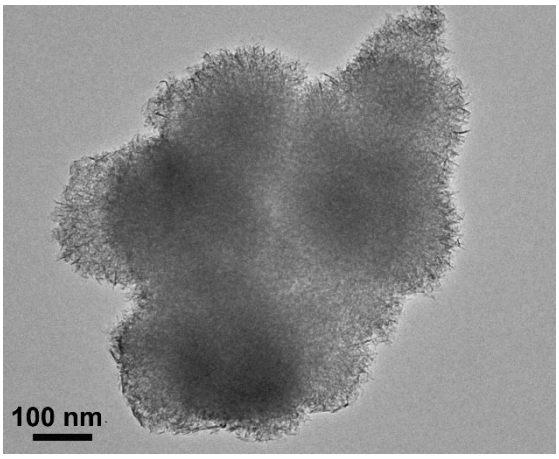

Figure S6. TEM image of solid manganese oxide prepared without $NH_4H_2PO_4$.

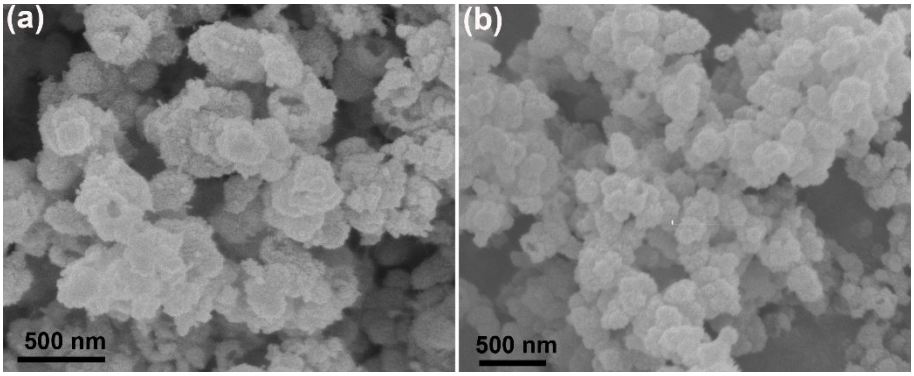

Figure S7. SEM images of h-MnO_xP_y prepared with (a) NaH_2PO_4 and (b) KH_2PO_4.

Table S2. Elemental compositions of h-Me-MnO_xP_y.

	Mn	**Co**	**Ni**	**Cu**	**O**	**P**
h-Co-MnO_xP_y	12.32	10.70	-[a]	-[a]	74.36	2.620
h-Ni-MnO_xP_y	11.87	-[a]	9.590	-[a]	75.55	2.990
h-Cu-MnO_xP_y	13.73	-[a]	-[a]	20.38	61.71	4.180

[a] *"-" : undetected*

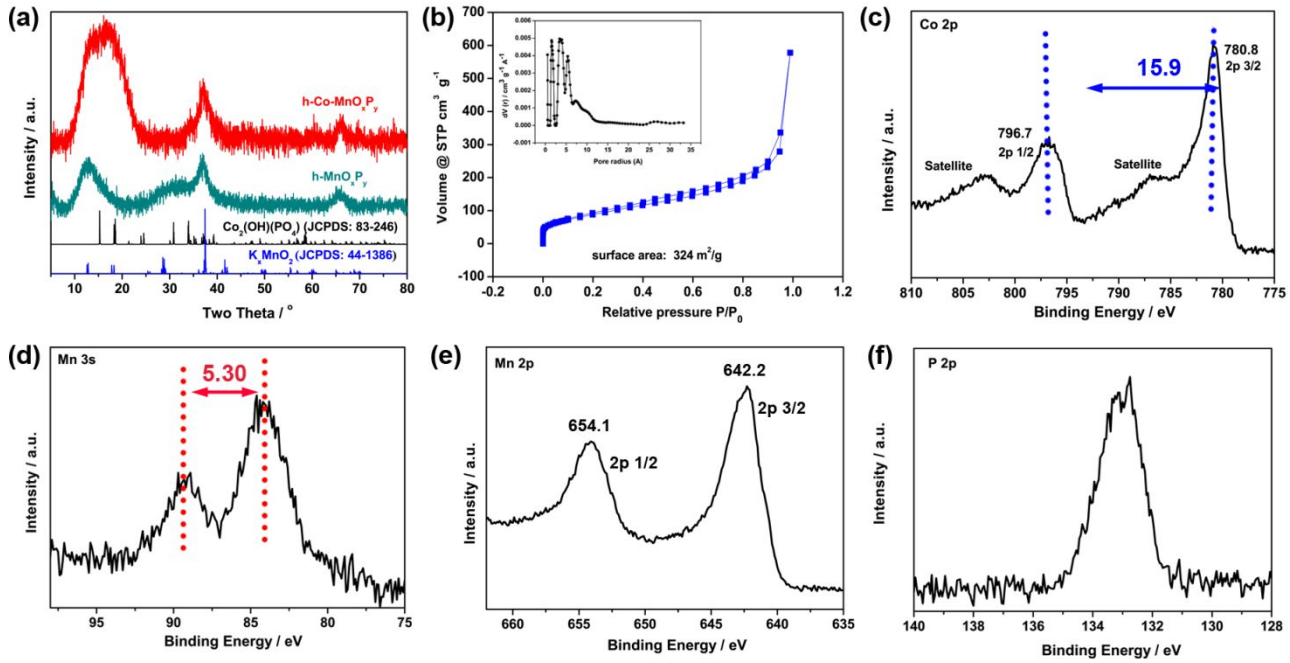

Figure S8. Microstructural characterizations of h-Co-MnO_xP_y. (a) XRD pattern, (b) N_2 adsorption/desorption isotherms with the pore distribution plot as an inset. (c) XPS Co 2p spectrum, (d) Mn 3s, (e) Mn 2p spectrum and (f) P 2p spectrum.

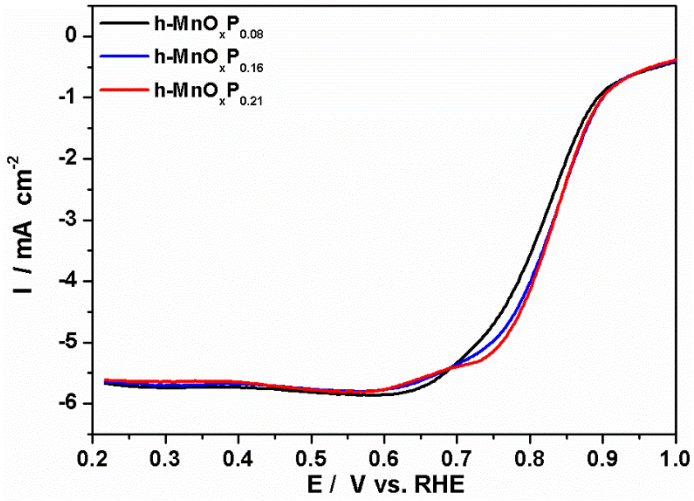

Figure S9. ORR activities in 0.1M KOH of h-MnO_xP_y with different phosphate contents.

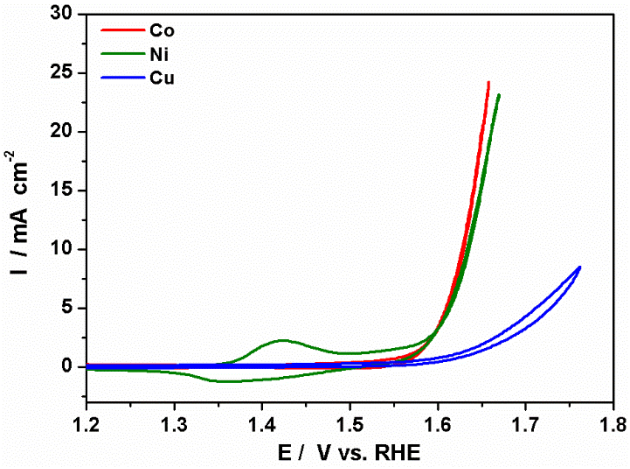

Figure S10. OER activities (iR-corrected) of different h-Me-$MnO_xP_{0.21}$ in 0.1 M KOH.

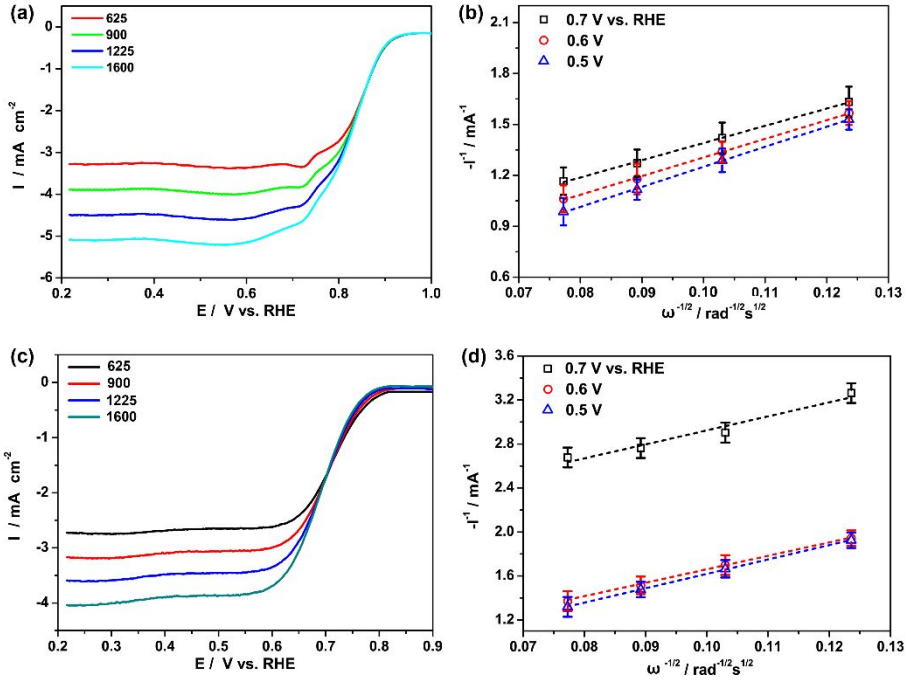

Figure S11. LSV measurements at different rotation speeds and the corresponding K-L plots at various potentials. (a), (b) for h-$MnO_xP_{0.21}$ and (c), (d) for h-Co-MnO_xP_y. All plots were corrected by CVs in N_2.

Table S3. Summary of noble-metal-free electrocatalysts for oxygen reduction reaction in 0.1 M KOH solution.

	$E_{1/2}$ (V *vs.* RHE)	Limiting current density (mA cm^{-2})	n	Reference
h-$MnO_xP_{0.21}$	**0.85**	**5.6**	**3.99**	**This work**
h-Co-$MnO_xP_{0.21}$	0.70	5.1	3.34	This work
20wt% Pt/C	0.84	5.4	4.01	This work
Cs-MnO_x-450/C	0.88	5.3	-[a]	[2]
α-MnO_2-SF/C	0.76	~5	4.2	[3]
Mn_xO_y/NC	0.81 (1 mA cm^{-2})	5	-[a]	[4]
c-$CoMn_2$/C	0.83	5.7	3.91	[5]
$MnCo_2O_4$/N-rmGO	0.85 (1 M KOH)	~3.8	~3.85	[6]
Co_3O_4/N-rmGO	0.83	~5	~4.0	[7]
meso/micro-PoPD	0.85	4.32	3.5	[8]
N-CNT	0.84	~0.3 mA	3.9	[9]
NPMC-1000	0.85	~6	~4.0	[10]

[a] *"-": no available literature data.*

Table S4. Summary of noble-metal-free electrocatalysts for oxygen evolution reaction in 0.1 M KOH solution.

	E_{onset} (V *vs.* RHE)	$E_{10mA\ cm-2}$ (V *vs.* RHE)	Tafel slope	Reference
h-Co-MnO_xP_y	**1.55**	**1.60**	**64.5**	**This work**
20wt% Ir/C	1.51	1.61	47.2	This work
Co@Co_3O_4/NC	0.88	1.64	-[a]	[10]
Co_xO_y/NC	~1.55	1.66	-[a]	[4]
ZIF derived carbon frameworks	~1.48	1.60	93	[15]
c-CoMn2/C	1.60	1.78	-[a]	[5]
(Pr0.5Ba0.5)CoO_3	~1.46	1.56	60	[13]
ultrathin $CoSe_2$ nanosheet	~1.50	1.55	44	[14]
CoMn LDH	1.45 (1 M KOH)	1.55(1 M KOH)	43	[15]
Ni_2P nanoparticles	1.45 (1 M KOH)	1.52(1 M KOH)	47	[16]
$Fe_{0.5}Co_{0.5}O_x$/NrGO	1.45 (1 M KOH)	1.49 (1 M KOH)	30.1	[17]

[a] "-": no available literature data.

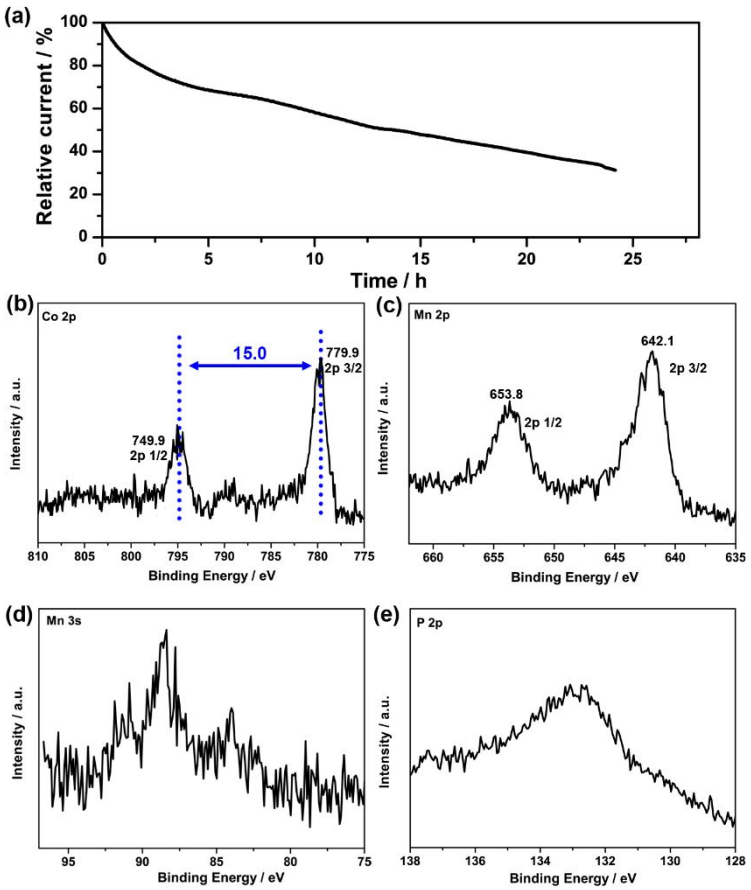

Figure S12 (a) Chronoamperogram (as % retention of initial current vs. time) of h-Co-$MnO_xP_{0.21}$ at 1.60 V vs. RHE. (b) the Co 2p, (c) Mn 2p, (d) Mn 3s and (e) P 2p XPS spectrum of h-Co-$MnO_xP_{0.21}$ after the extended stability tests.

An extended (24 h) OER stability test of h-Co-$MnO_xP_{0.21}$ was also conducted. As shown in Figure S12a, the current density gradually decreased during the test, retaining only 30% of its initial value after the test. The cause for the activity loss was inferred from the XPS analysis of the chemical states of h-Co-$MnO_xP_{0.21}$ after the test. The Co 2p spectrum (Figure S12b) of the post-test sample was different from the h-Co-$MnO_xP_{0.21}$ before the test (Figure S8c). Two peaks were detected but without the satellite features. The 15.0 eV peak separation is smaller than that of h-Co-$MnO_xP_{0.21}$ before the test (15.9 eV). As the Co 2p spectrum bears similarity to that of CoOOH, oxidation of Co (II) to Co (III) likely occurred during the extended OER test. The Mn 2p spectrum (Figure S12c) of h-Co-$MnO_xP_{0.21}$ after the stability test still showed the same two broad peaks as in the sample before (Figure S8d). The intensity of the Mn 3s signal (Figure S12d) was however substantially reduced to suggest the loss of Mn from the catalyst during the test. The P 2p spectrum (Figure S12e) was broadened after the test concomitant with a general intensity decrease, which we have taken as an indication of PO_4^{3-} dissolution from the catalyst. The post-test XPS measurements therefore indicated changes to the h-Co-$MnO_xP_{0.21}$ surface structure which could be the cause for the decreased OER activity.

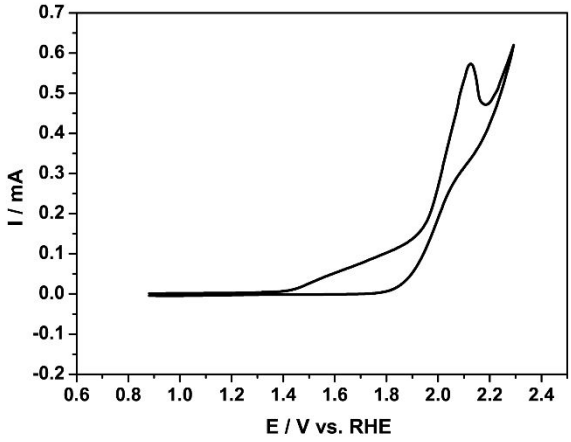

Figure S13. Voltammogram of h-Co-$MnO_xP_{0.21}$ on an ITO glass in 0.1 M KOH solution.

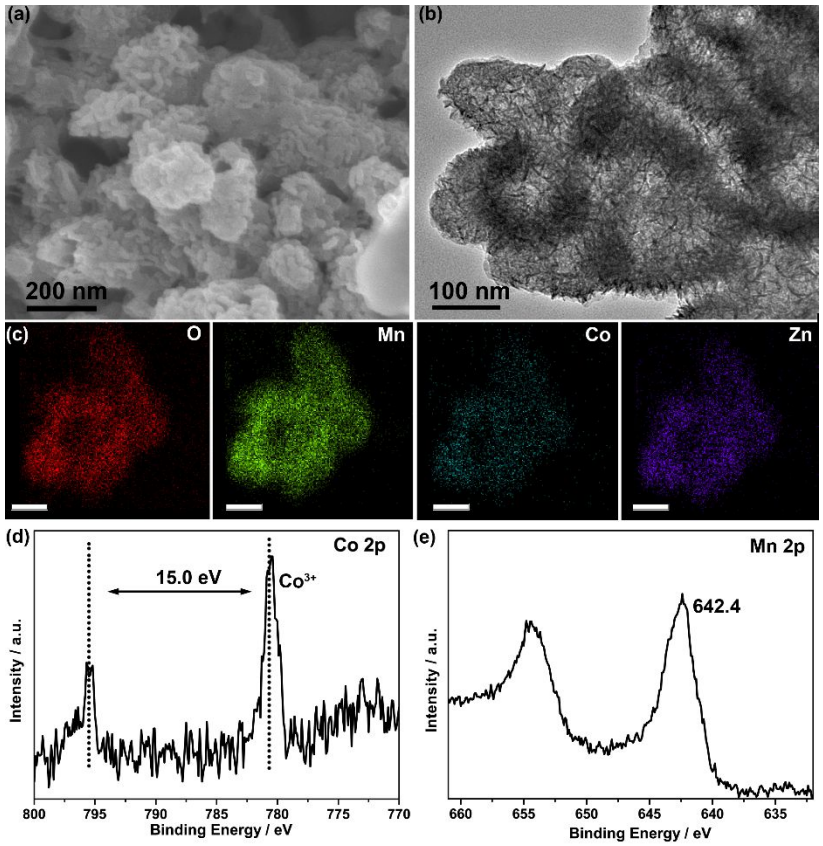

Figure S14. (a) SEM, (b) TEM image (c) EDS elemental maps, (d) Co 2p XPS and (e) Mn 2p XPS of the h-$MnO_xP_{0.21}$ + h-Co-$MnO_xP_{0.21}$ catalysts after an extended operation of a rechargeable alkaline Zn-air battery

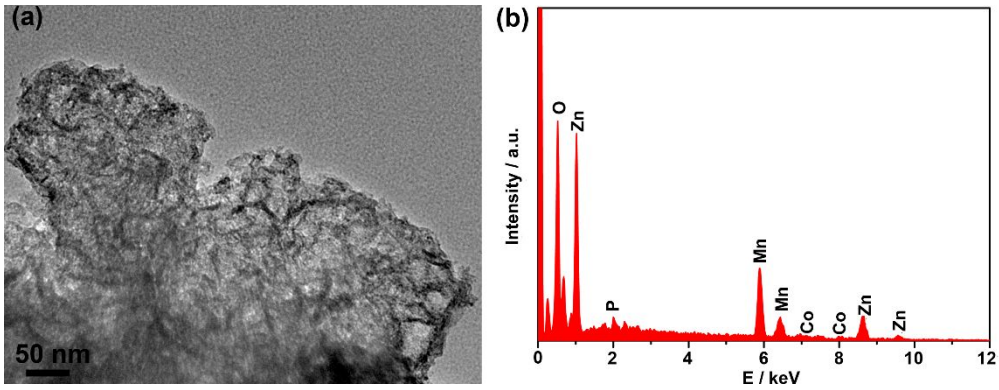

Figure S15. (a) TEM image and (b) EDS analysis of the h-$MnO_xP_{0.21}$ + h-Co-MnO_xP_y combined catalyst system after the prolonged operation of a neutral rechargeable Zn-air battery.

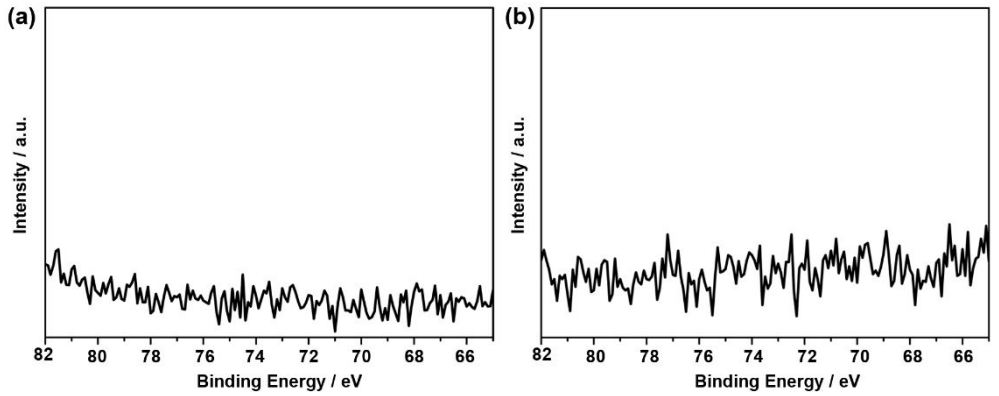

Figure S16. Pt 4f XPS spectrum of (a) h-$MnO_xP_{0.21}$ and (b) h-Co-$MnO_xP_{0.21}$ after OER stability tests in a 3-electrode cell with a Pt foil counter electrode. Pt signal was not detected in both samples.

Table S5. Summary of the performance of rechargeable Zn-air batteries.

Catalysts	Electrolyte	Charge/discharge voltage gap (V)	Stability	Reference
h-$MnO_xP_{0.21}$ + h-Co-MnO_xP_y	**6.0 M KOH +0.1 M $ZnCl_2$**	**~0.72 at 5 mA cm^{-2}**	**1h/cycle for 90 cycles; voltage gap increased ~0.13 V**	**This work**
20wt% Pt/C + 20wt% Ir/C	6.0 M KOH +0.1 M $ZnCl_2$	~0.72 at 5 mA cm^{-2}	1h/cycle for 90 cycles; voltage gap increased ~0.19 V	This work
CoO/NCNT+Ni Fe LDH	6.0 M KOH + 0.2 M $Zn(Ac)_2$	~0.6 at 5 mA cm^{-2}	200s/cycle for 3.3h; no significant voltage change	18
macro/meso-NC-NH_3 + COMT@Ni	6.0 M KOH +0.2 M $ZnCl_2$	~0.7 at 10 mA cm^{-2}	2h/cycle for 200 cycles; voltage gap increased ~0.11 V	19
Atomic Co–N_x– doped graphene	6.0 M KOH + 0.2 M $ZnCl_2$	~1.0 at 5 mA cm^{-2}	20 min/cycle for 180 cycles; voltage gap increased ~0.12 V	20
NPMC-1000	6.0 M KOH	~1.75 at 2 mA cm^{-2}	10 min/cycle for 180 cycles; voltage gap increased ~0.7 V	10
NCNT/CoO-NiONiCo	6.0 M KOH + 0.2 M $ZnCl_2$	~0.86 at 20 mA cm^{-2}	10 min/cycle for 100 cycles; negligible change	21
Meso/micro-FeCo-N_x-30	6.0 M KOH + 0.2 M $Zn(Ac)_2$	~0.80 at 10 mA cm^{-2}	2h/cycle for 40h, negligible change	17

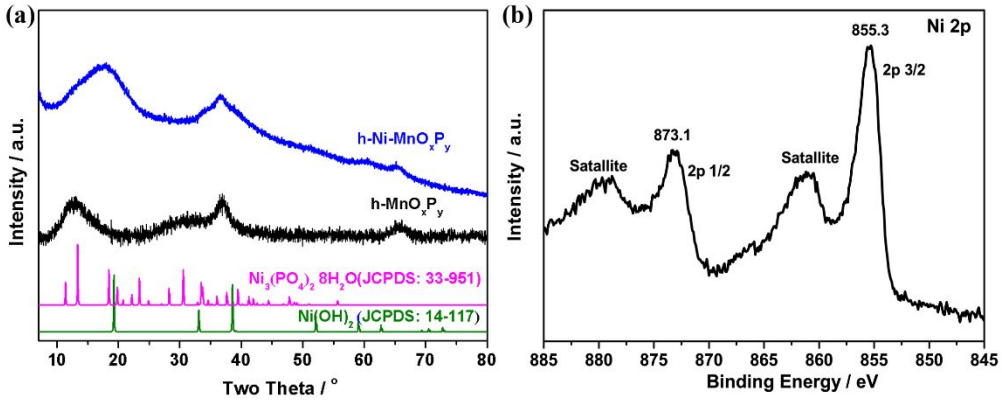

Figure S17. (a) XRD pattern and (b) XPS Ni 2p spectrum of h-Ni-MnO_xP_y.

Figure S10 also shows the good OER performance of h-Ni-$MnO_xP_{0.21}$. This could be attributed to the existence of Ni (II) in the catalyst. Relative to h-$MnO_xP_{0.21}$, the XRD pattern of h-Ni-$MnO_xP_{0.21}$ (Figure S16a) exhibited a broad feature around 2θ = 10-25° to suggest the presence of nickel hydroxide or nickel phosphate. In the Ni 2p XPS spectrum of h-Ni-$MnO_xP_{0.21}$ in Figure S16b, the two characteristic peaks at 855.3 and 873.1 eV with shoulders correspond well with the $2p_{3/2}$, $2p_{1/2}$ states of Ni (II) and their satellites. Since it is known that nickel (II) can exhibit very good OER performance in alkaline solution,[22-23] the good OER activity of h-Ni-$MnO_xP_{0.21}$ may also have originated from its Ni(II) content.

References

(1) Lima, F. H. B.; Calegaro, M. L.; Ticianelli, E. A., Electrocatalytic activity of manganese oxides prepared by thermal decomposition for oxygen reduction. *Electrochim. Acta* **2007,** *52*, 3732-3738.

(2) Mosa, I. M.; Biswas, S.; El-Sawy, A. M.; Botu, V.; Guild, C.; Song, W.; Ramprasad, R.; Rusling, J. F.; Suib, S. L., Tunable mesoporous manganese oxide for high performance oxygen reduction and evolution reactions. *J. Mater. Chem. A* **2016,** *4*, 620-631.

(3) Meng, Y.; Song, W.; Huang, H.; Ren, Z.; Chen, S. Y.; Suib, S. L., Structure-property relationship of bifunctional MnO_2 nanostructures: highly efficient, ultra-stable electrochemical water oxidation and oxygen reduction reaction catalysts identified in alkaline media. *J. Am. Chem. Soc.* **2014,** *136*, 11452-11464.

(4) Masa, J.; Xia, W.; Sinev, I.; Zhao, A.; Sun, Z.; Grutzke, S.; Weide, P.; Muhler, M.; Schuhmann, W., Mn_xO_y/NC and Co_xO_y/NC nanoparticles embedded in a nitrogen-doped carbon matrix for high-performance bifunctional oxygen electrodes. *Angew. Chem. Int. Ed.* **2014,** *53*, 8508-8512.

(5) Li, C.; Han, X.; Cheng, F.; Hu, Y.; Chen, C.; Chen, J., Phase and composition controllable synthesis of cobalt manganese spinel nanoparticles towards efficient oxygen electrocatalysis. *Nat. Commun.* **2015,** *6, 7345.*

(6) Liang, Y. Y.; Wang, H. L.; Zhou, J. G.; Li, Y. G.; Wang, J.; Regier, T.; Dai, H. J., Covalent Hybrid of Spinel Manganese-Cobalt Oxide and Graphene as Advanced Oxygen Reduction Electrocatalysts. *J. Am. Chem. Soc.* **2012,** *134*, 3517-3523.

(7) Liang, Y. Y.; Li, Y. G.; Wang, H. L.; Zhou, J. G.; Wang, J.; Regier, T.; Dai, H. J., Co_3O_4 nanocrystals on graphene as a synergistic catalyst for oxygen reduction reaction. *Nat. Mater.* **2011,** *10*, 780-786.

(8) Liang, H. W.; Zhuang, X.; Bruller, S.; Feng, X.; Mullen, K., Hierarchically porous carbons with optimized nitrogen doping as highly active electrocatalysts for oxygen reduction. *Nat. Commun.* **2014,** *5*, 4973.

(9) Gong, K. P.; Du, F.; Xia, Z. H.; Durstock, M.; Dai, L. M., Nitrogen-Doped Carbon Nanotube Arrays with High Electrocatalytic Activity for Oxygen Reduction. *Science* **2009,** *323*, 760-764.

(10) Zhang, J.; Zhao, Z.; Xia, Z.; Dai, L., A metal-free bifunctional electrocatalyst for oxygen reduction and oxygen evolution reactions. *Nat. Nanotech.* **2015,** *10*, 444-452.

(11) Aijaz, A.; Masa, J.; Rösler, C.; Xia, W.; Weide, P.; Botz, A. J.; Fischer, R. A.; Schuhmann, W.; Muhler, M., $Co@Co_3O_4$ Encapsulated in Carbon Nanotube-Grafted Nitrogen-Doped Carbon Polyhedra as an Advanced Bifunctional Oxygen Electrode. *Angew. Chem. Int. Ed.* **2016,** *55*, 4087-4091.

(12) Xia, B. Y.; Yan, Y.; Li, N.; Wu, H. B.; Lou, X. W.; Wang, X., A metal–organic framework-derived bifunctional oxygen electrocatalyst. *Nat. Energy.* **2016,** *1*, 15006.

(13) Grimaud, A.; May, K. J.; Carlton, C. E.; Lee, Y.-L.; Risch, M.; Hong, W. T.; Zhou, J.; Shao-Horn, Y., Double perovskites as a family of highly active catalysts for oxygen evolution in alkaline solution. *Nat. Commun.* **2013,** *4, 2439*.

(14) Liu, Y.; Cheng, H.; Lyu, M.; Fan, S.; Liu, Q.; Zhang, W.; Zhi, Y.; Wang, C.; Xiao, C.; Wei, S.; Ye, B.; Xie, Y., Low overpotential in vacancy-rich ultrathin $CoSe_2$ nanosheets for water oxidation. *J. Am. Chem. Soc.* **2014,** *136*, 15670-15675.

(15) Song, F.; Hu, X., Ultrathin cobalt-manganese layered double hydroxide is an efficient oxygen evolution catalyst. *J. Am. Chem. Soc.* **2014,** *136*, 16481-16484.

(16) Stern, L. A.; Feng, L.; Song, F.; Hu, X., Ni_2P as a Janus catalyst for water splitting: the oxygen evolution activity of Ni_2P nanoparticles. *Energy Environ. Sci.* **2015,** *8*, 2347-2351.

(17) Wei, L.; Karahan, H. E.; Zhai, S.; Liu, H.; Chen, X.; Zhou, Z.; Lei, Y.; Liu, Z.; Chen, Y., Amorphous Bimetallic Oxide–Graphene Hybrids as Bifunctional Oxygen Electrocatalysts for Rechargeable Zn–Air Batteries. *Adv. Mater.* **2017,** *29*, 1701410.

(18) Li, Y.; Gong, M.; Liang, Y.; Feng, J.; Kim, J.-E.; Wang, H.; Hong, G.; Zhang, B.; Dai, H., Advanced zinc-air batteries based on high-performance hybrid electrocatalysts. *Nat. Commun.* **2013,** *4*, 1805.

(19) Li, L.; Liu, C.; He, G.; Fan, D.; Manthiram, A., Hierarchical pore-in-pore and wire-in-wire catalysts for rechargeable Zn– and Li–air batteries with ultra-long cycle life and high cell efficiency. *Energy Environ. Sci.* **2015,** *8*, 3274-3282.

(20) Tang, C.; Wang, B.; Wang, H. F.; Zhang, Q., Defect Engineering toward Atomic Co–N_x–C in Hierarchical Graphene for Rechargeable Flexible Solid Zn-Air Batteries. *Adv. Mater.* **2017,** *29*, 1703185.

(21) Liu, X.; Park, M.; Kim, M. G.; Gupta, S.; Wu, G.; Cho, J., Integrating NiCo alloys with their oxides as efficient bifunctional cathode catalysts for rechargeable zinc–air batteries. *Angew. Chem. Int. Ed.* **2015,** *54*, 9654-9658.

(22) Stern, L. A.; Hu, X., Enhanced oxygen evolution activity by NiO_x and $Ni(OH)_2$ nanoparticles. *Faraday Discuss.* **2014,** *176*, 363-379.

(23) Zhan, Y.; Lu, M.; Yang, S.; Xu, C.; Liu, Z.; Lee, J. Y., Activity of Transition-Metal (Manganese, Iron, Cobalt, and Nickel) Phosphates for Oxygen Electrocatalysis in Alkaline Solution. *ChemCatChem* **2016,** *8*, 372-379.